

On the hierarchical triple nature of the former red nova precursor candidate KIC 9832227

Geza Kovacs¹, Joel D. Hartman², and Gáspár Á. Bakos^{2,3,4}

¹ Konkoly Observatory of the Hungarian Academy of Sciences, Budapest, 1121 Konkoly Thege ut. 15-17, Hungary
e-mail: kovacs@konkoly.hu

² Department of Astrophysical Sciences, Princeton University, NJ 08544, USA

³ Packard Fellow

⁴ MTA Distinguished Guest Fellow, Konkoly Observatory, Hungary

Received June 28, 2019 / Accepted ...

ABSTRACT

We revisit the issue of period variation of the recently claimed red nova precursor candidate KIC 9832227. By using the data gathered during the main mission of the Kepler satellite, those collected by ground-based wide-field surveys and other monitoring programs (such as ASAS-SN), we find that the currently available timing data strongly support a model consisting of the known W UMa binary and a distant low-mass companion with an orbital period of ~ 13.5 years. The period of the W UMa component exhibits a linear period decrease with a pace of $(1.10 \pm 0.05) \times 10^{-6}$ days per year, within the range of many other similar systems. This rate of decrease is several orders of magnitude lower than that of V1309 Sco, the first (and so far the only) well-established binary precursor of a nova observed a few years before the outburst. The high-fidelity fit of the timing data and the conformity of the derived minimum mass of $(0.38 \pm 0.02) M_{\odot}$ of the outer companion from these data with the limit posed by the spectroscopic non-detection of this component, are in agreement with the suggested hierarchical nature of this system.

Key words. binaries: close – binaries: eclipsing – binaries: general – binaries: spectroscopic – stars: individual (KIC 9832227) – stars: variables: general

1. Introduction

Merging stars, degenerate objects and black holes have been thought for a long time to be responsible for many energetic phenomena in the Universe (e.g., for a subclass of Type I supernovae: Kuncarayakti 2016, Podsiadlowski, Joss & Hsu et al. 1992, Truran & Cameron 1971). The discovery of the first black hole merger by the LIGO collaboration in 2015 (Abbott et al. 2016) highlighted further the significance of the merger events. At the less energetic side, there is the recently discovered group of optical transients in between supernovae and novae. The group, annotated as Luminous Red Novae, consists of only a handful of objects, and they are suspected to be the result of low-mass stellar merging after the common envelope phase (e.g., Pastorello et al. 2019, Pejcha et al. 2017). Unlike in the case of black holes, for stars, during the precursor period of the actual merging event, there is a chance to spot potential mergers on the basis of the size of the period decrease. Unfortunately, nova events are rare, and their pre-discovery requires intensive monitoring. So far, there is only one object that has been clearly identified with this method. Thanks to the serendipitous overlap of the early OGLE survey area toward the Galactic Center with the position of Nova Scorpii 2008 (Nakano, Nishiyama & Kabashima 2008, Mason et al. 2010), Tyndel et al. (2011) was able to identify V1309 Sco as a possible progenitor of the nova and trace back both the light curve and the variation of the orbital period. This has resulted in a wonderful match between the overall brightening and the dramatic period decrease, and thereby providing direct evidence for the first time of the viability of the binary connection with the red nova events (see also the possi-

ble settling of the system in a blue straggler state some 10 years after the outburst – Ferreira et al. 2019).

Stimulated by the case of V1309 Sco, Molnar et al. (2017) investigated the W UMa system KIC 9832227 by using their own data combined by those of the Kepler satellite and wide-field surveys from earlier epochs. They found that the eclipse timing variation was similar in nature to that of V1309 Sco, and, from the exponential trend they predicted a likely nova explosion in 2022. The study heavily relied on a single point from an earlier epoch, that was shown to suffer from an unfortunate timing typo (Socia et al. 2018). This has cast doubt on the merger hypothesis, and, because of the poor observational coverage, vaguely suggested a different origin of the timing variation, including the presence of a tertiary component. The purpose of the present work is to elucidate further the status of KIC 9832227 by using both so far unpublished data and publicly available archival observations. This work not only confirms the result of Socia et al. (2018) on the lack of strong overall period change, but yields also valuable support to the hierarchical model of the system.

2. Datasets, derived O-C values

In revisiting the timing properties of KIC 9832227, we searched for additional sources of data to: i) cover the crucial period prior to $T_0 = \text{JD } 2455000.0$ more densely; ii) extend the time span past 2017; iii) fill in as densely as possible also other parts of the time interval covered by any data available (we found this latter step also necessary, since not all the data employed in the former studies are readily available at this moment).

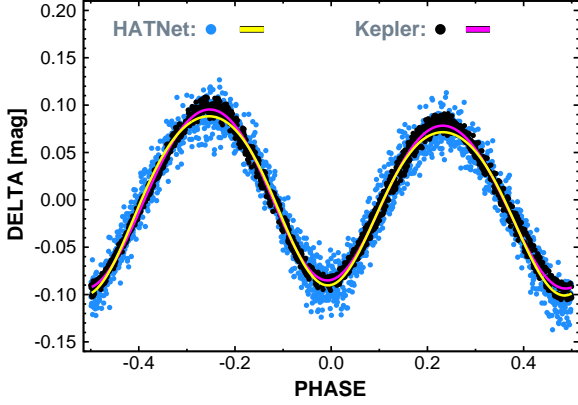


Fig. 1. Comparison of the folded light curves and the corresponding 4-th order Fourier fits (continuous lines) for the HATnet and Kepler observations on KIC 9832227. We use the adjacent datasets corresponding to $T_{\text{mid}} = 875$ and 878, as given in Table 1. The ephemeris used is given in the same table. To avoid crowdedness, only every 2-nd data points are plotted.

Importantly, the HATNet¹ survey (Bakos et. al. 2004) covered the Kepler field and we have a substantial amount of data available both in the pre- and post- T_0 periods. The earlier set from HATNet is between the observations made by the Vulcan telescope (Borucki et al. 2001, Socia et al. 2018) and those gathered by Kepler in the beginning of the mission. We also have data obtained during the second part of the mission, establishing a good basis of comparison of the two datasets of highly different quality.² Somewhat surprisingly, for the purpose of this study, the two datasets are quite compatible, as it is demonstrated in Fig. 1. Interestingly, the depth of the primary minimum near phase zero is shallower than that of the secondary minimum. In other epochs this may change, likely because of stellar activity and binary interaction (Socia et al. 2018). Because of these effects, we have a non-stationary light curve, yielding somewhat fuzzy segmented folded light curves also for the observations made by Kepler. For HATNet the higher observational noise further increases the scatter, but it is still tolerable for the goal of this work, i.e., deriving moments of the primary minima with an accuracy of ~ 1 min.

Throughout this work we use light curves (LCs) obtained by simple ensemble photometry. For high-precision photometric time series analysis, application of filtering methods that clean up the data from colored noise play a crucial role in the full utilization of the signal content of the time series (i.e., see Kovacs et al. 2005, Tamuz et al. 2005, Bakos et al. 2010, Smith et al. 2012). Our decision to stay with the more standard photometric data stems from the following reasons: i) Not all datasets contain these filtered LCs (e.g., ASAS-SN); ii) Since the amplitude of the light variation is large compared to that of the colored noise, the application of these filtering methods should consider this fact, otherwise the filtered signals will be distorted (see Kovacs 2018). The systematics-filtered LCs, available at the download sites do not have a proper correction for this effect; iii) Tests made with systematics-filtered LCs as given at the download sites (i.e., not containing the signal reconstruction feature

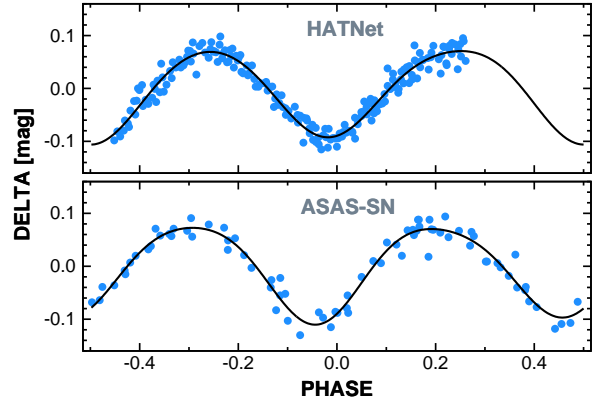


Fig. 2. Examples of the performance of the fourth order Fourier fit (continuous line) for partially and sparsely covered cases. The light curves shown correspond to the datasets of $T_{\text{mid}} = 998$ and $T_{\text{mid}} = 1840$ as given in Table 1.

listed in ii) yield epochs within the error limits of the values derived from the ensemble photometric data.

To further boost the coverage of the period variation, we made a thorough search among other survey projects, including space missions. This search ended up with data sources from the infrared survey satellite WISE (Wright et al. 2010) through the ASAS-SN supernova search program (Shappee et al. 2014 and Kochanek et al. 2017) to the inventory of AAVSO. The detailed description of the datasets used is given in Appendix A.

In dividing the data into segments of appropriate length to avoid smearing of the O-C values due to long individual time bases, we inspected the datasets separately and made a decision case-by-case. As a result, the time bases vary by several factors from one dataset to the other. Because of excessive errors, or improper phase coverage, certain observations – although available – were not used (e.g., data from the Palomar Transient Factory project – see Rau et al. 2009 and Law et al. 2009). In the other extreme, for the Kepler data, we could go almost with a daily time base, but it would not serve any good for the purpose of the long-term study of our target. Nevertheless, it is worthwhile to note that such a study has certainly a relevance also from our point of view, since it is indicative of the inherent O-C jitter likely attributed to stellar activity. The analysis made by Socia et al. (2018) shows that the RMS of this physical scatter is about 1–2 min on a time scale of several tens of days. As a result, for the Kepler data we use segments of ~ 80 d, and avoid mixing various quarters, if they show visible zero point differences.

It is important to choose a proper method to find the optimum way to estimate the epochs of the primary minima. Because of the varying light curve, this task is not entirely trivial, even though the basic light variation, originating from the eclipses of this W UMa-type system, is decomposable into a Fourier sum of a few components only. We followed a simple empirical approach to select the best method. From the five proposed methods we selected the one that yielded the smallest residual scatter for the few-parameter O-C model to be described in detail in Sect. 3. The following methods have been proposed (we also show the identifier of the O-C value corresponding to these methods as labelled in Table 1).

- (a) *Fourier fit I* – OC1: Fourth-order Fourier fit to the entire phase-folded light curve (as given on a certain timebase) and search for the primary minimum by using the densely-sampled synthetic light curve.

¹ <https://hatnet.org/>

² The photometric time series from the HatNet project is available at the CDS via anonymous ftp to cdsarc.u-strasbg.fr (130.79.128.5) or via <http://cdsarc.u-strasbg.fr/viz-bin/qcat?J/A+A/vol/page>

- (b) *Fourier fit II* – OC2: As in (a), but search for the moment of the secondary eclipse and shift the value by half of the period (we recall that the secondary eclipses are in many cases deeper than the primary eclipses, therefore, it is not entirely a bold idea to use these events to predict the moments of the primary eclipse – with the assumption of circular binary orbit).
- (c) *Fourier fit I+II* – OC3: This is just a simple average of the O-C values obtained by (a) and (b).
- (d) *Template fit Ia* – OC4: Use some ‘representative’ light curve as a template and perform a simple residual minimization on the full orbital phase by shifting this template relative to the target time series. If the template is properly chosen, the amount of shift will be characteristic of the overall shift of the light curve, perhaps depending in a less extent on the temporal change in its shape. The template is generated by the Fourier fits in running the minimum search by method (a).
- (e) *Template fit Ib* – OC5: As in (d), but the RMS of the residual is calculated only in a restricted range of the phase of the primary minimum (in our case this is ± 0.1 in the units of the orbital period).

In the O-C estimates based on Fourier fits and in the calculation of the templates for methods (d) and (e), the individual time series $X(i)$ are fitted with a low order Fourier sum of

$$X(i) = A_0 + \sum_{j=1}^m A_j \sin(2\pi j(t_i - t_0)/P_0 + \varphi_j), \quad (1)$$

where $t_0 = 2454953.949183$, $P_0 = 0.4579515$. This ephemeris, given by Socia et al. (2018) ensures to remain compatible with the earlier investigations and yield near zero O-C value at HJD= 2455000.0. After experimenting with the Fourier order, we found that $m = 4$ yields a good representation of all subsets, including even those with modest or gapped coverage of the full folded light curve (see Fig. 2).

For O-C values of type (d) and (e), we need to select a ‘proper’ template that yields the best fit for our low parameter model with the O-C values derived with this favorable template. We present the test leading to our final choice in Sect. 3. Here we show only the Fourier fits to all the 37 data segments analyzed in this paper and the three pre-selected candidates for master template (see Fig. 3). To aid the template testing – i.e., to have an overall view on the light curve morphology when selecting some subset of the light curves – the synthetic Fourier light curves have been ordered by the following algorithm.

Starting with any of the light curves with some serial index $i \in [1, n]$, where n is the number of light curves (in our case 37), we find the ‘closest’ neighbor to this light curve; i.e., we search for the light curve yielding the smallest RMS of the residuals obtained after subtracting the two time series from each other. We denote this RMS between the i -th test template and its nearest neighbor of serial index j by $\sigma(i, j)$. Then, this ‘closest neighbor’ is searched for its closest neighbor (excluding of course all the previously found close neighbors). We continue the search until the last closest neighbor is found. The mutual RMS values $\{\sigma(i, k)\}$ are examined and their variance is computed: $\sigma^2(i) = \frac{1}{n} \sum_{k=1}^n (\sigma(i, k) - \langle \sigma(i, k) \rangle)^2$, where $\langle \sigma(i, k) \rangle = \frac{1}{n} \sum_{k=1}^n \sigma(i, k)$. The degree of smoothness of the ordering derived from the above search for the i -th test template is then characterized by $\sigma(i)$. We repeat this whole process with the next starting template and do it for all possible starting templates. The smoothness parameters $\{\sigma(i)\}$ for these orderings are examined, and the one with the

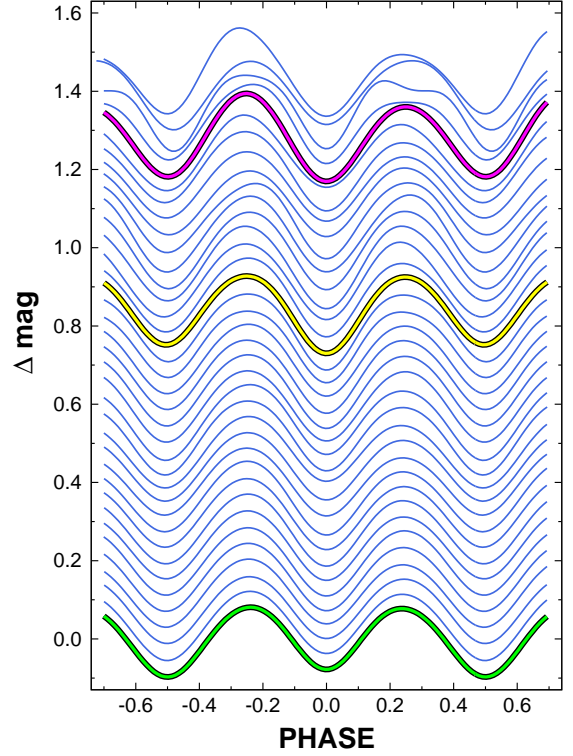


Fig. 3. Fourier-fitted synthetic light curves of all the 37 data segments analyzed in this paper. The primary minima are shifted to zero phase. The time series are ordered on the basis of the closest neighbor as described in Sect. 2. The pre-selected templates are shown by distinct colors. Following the notation of Table 1, the green, yellow and magenta lines show the Fourier fits corresponding to segments *Kepler-4*, *AAVSO-V-1* and *AAVSO-V-4*, respectively.

smallest value is selected (with the associated starting template and ordering).

By using this algorithm we obtained the light curves shown in Fig. 3 with the set *Kepler-4* as the starting template. It is clear that most of the light curves are very similar to each other, and that there are only ~ 4 data segments that do not fit the overall smooth morphological sequence. These segments are *AAVSO-V-2*, *WISE-W12*, *HAT-5* and *WASP-1* (see the top four light curves in Fig. 3).

We summarize the datasets used and the O-C values derived in Table 1. The errors of the moments (eOC#) of the mid-eclipses have been computed from a simple Monte Carlo test. In the case of the moments derived from Fourier fits for the given subset, the best fit Fourier signal is perturbed by a realization of a Gaussian noise with the standard deviation obtained by the fit to the real data. Then, this mock signal is fitted in the same way as the real data and the moment of the mid-eclipse is stored. The process is repeated thousand times and the standard deviation of the moments of these mid-eclipse values is considered as the error of the moment of the observed eclipse. For the eclipse times derived from template fitting the procedure is the same, except for the second step, when, instead of fitting a Fourier sum to the mock signal, we use a template.

The O-C data presented in Table 1 are plotted in Fig. 4. It is worthwhile to emphasize that 3σ error bars are used, since standard 1σ bars would not be visible in most cases. It is also noted

Table 1. Times of the primary minima for KIC 9832227.

$T_{\text{obs}}(1)$ (BJD ¹)	T_{mid} (d)	ΔT (d)	OC1 (min)	eOC1 (min)	OC2 (min)	eOC2 (min)	OC3 (min)	eOC3 (min)	OC4 (min)	eOC4 (min)	OC5 (min)	eOC5 (min)	Source ¹
1451.56499	-3549	176	41.5	2.7	41.2	3.1	41.4	2.4	38.2	1.3	33.6	2.0	<i>NSVS-12</i>
2838.22900	-2162	45	22.6	2.0	22.6	2.0	22.6	2.0	22.6	2.0	22.6	2.0	<i>Vulcan</i>
3134.06377	-1867	5	19.9	3.3	19.4	3.2	19.7	2.6	14.5	1.6	13.2	3.1	<i>WASP-1</i>
3188.09813	-1813	35	14.2	0.4	12.9	0.4	13.6	0.3	13.8	0.2	12.5	0.4	<i>HAT-1</i>
3280.14596	-1721	65	13.6	0.4	13.4	0.5	13.5	0.4	13.2	0.3	11.9	0.4	<i>HAT-2</i>
3584.67982	-1416	49	8.0	0.3	7.4	0.4	7.7	0.3	7.9	0.3	7.3	0.4	<i>HAT-3</i>
4183.21603	-817	299	-1.1	3.2	0.3	4.4	-0.4	3.0	-0.0	2.0	2.6	3.1	<i>ASAS-IV</i>
4263.81717	-737	33	1.3	0.7	-4.5	0.7	-1.6	0.6	-2.6	0.4	1.3	0.5	<i>WASP-3</i>
4647.12158	-353	41	-0.1	0.4	-3.4	0.5	-1.8	0.4	-2.6	0.3	-1.3	0.4	<i>WASP-4</i>
4994.24732	-6	40	-2.3	0.5	-5.9	0.6	-4.1	0.4	-4.0	0.3	-1.3	0.5	<i>Kepler-1</i>
5073.93207	74	38	-0.6	0.5	-6.6	0.6	-3.6	0.5	-4.0	0.3	-0.0	0.4	<i>Kepler-2</i>
5147.65928	147	34	-4.9	0.5	-2.0	0.6	-3.4	0.4	-3.3	0.3	-4.6	0.5	<i>Kepler-3</i>
5321.68220	322	37	-2.9	0.5	-3.1	0.5	-3.0	0.4	-2.6	0.3	-2.6	0.6	<i>Kepler-4</i>
5397.70233	398	38	-2.7	0.2	-5.6	0.3	-4.1	0.2	-4.6	0.3	-2.0	0.3	<i>Kepler-5</i>
5408.69213	408	91	-4.1	2.2	8.9	3.2	2.4	2.2	-2.6	2.1	-4.0	3.4	<i>WISE-W12</i>
5473.72165	473	37	-3.6	0.4	-4.4	0.4	-4.0	0.4	-4.0	0.2	-3.3	0.5	<i>Kepler-6</i>
5557.98516	558	46	-2.9	0.5	-7.8	0.5	-5.4	0.4	-5.3	0.3	-2.0	0.5	<i>Kepler-7</i>
5644.99354	645	40	-6.4	0.3	-6.9	0.3	-6.6	0.2	-6.6	0.2	-5.9	0.2	<i>Kepler-8</i>
5722.38858	722	37	-4.6	0.3	-11.0	0.3	-7.8	0.2	-7.9	0.3	-3.3	0.3	<i>Kepler-9</i>
5797.95109	798	38	-3.9	0.2	-9.0	0.2	-6.4	0.2	-6.6	0.0	-3.3	0.3	<i>Kepler-10</i>
5820.84780	821	27	-5.1	0.3	-8.9	0.3	-7.0	0.2	-6.6	0.1	-4.6	0.3	<i>HAT-4a</i>
5875.34399	875	39	-5.2	0.2	-9.0	0.5	-7.1	0.3	-6.6	0.2	-4.6	0.3	<i>Kepler-11</i>
5877.63486	878	28	-3.6	0.3	-8.7	0.4	-6.2	0.3	-5.9	0.2	-3.3	0.4	<i>HAT-4b</i>
5998.07105	998	1	-10.8	1.9	1.6	11.4	-4.6	6.3	-7.9	1.0	-7.3	1.7	<i>HAT-5</i>
6140.03581	1140	32	-11.1	0.3	-14.6	0.2	-12.9	0.2	-12.5	0.1	-9.2	0.2	<i>Kepler-12</i>
6214.22294	1214	41	-12.6	0.2	-15.2	0.2	-13.9	0.2	-13.8	0.1	-10.6	0.3	<i>Kepler-13</i>
6298.48454	1298	43	-14.7	0.2	-17.8	0.2	-16.2	0.1	-15.8	0.0	-12.5	0.3	<i>Kepler-14</i>
6382.74892	1383	40	-12.8	0.2	-18.1	0.2	-15.5	0.1	-15.2	0.2	-9.9	0.1	<i>Kepler-15</i>
6840.23198	1840	139	-27.9	2.9	-27.2	3.4	-27.6	2.6	-28.4	1.7	-25.1	3.3	<i>ASAS-SN-1</i>
7201.09114	2201	132	-37.4	5.3	-39.4	4.5	-38.4	3.9	-39.6	1.9	-33.0	3.2	<i>ASAS-SN-2</i>
7336.64185	2336	7	-41.7	0.3	-44.7	0.3	-43.2	0.2	-45.5	0.2	-33.6	0.3	<i>AAVSO-V-1</i>
7569.73270	2569	132	-51.0	4.9	-53.2	3.7	-52.1	3.2	-52.1	1.7	-39.6	4.2	<i>ASAS-SN-3</i>
7906.77350	2907	60	-67.5	0.4	-67.5	0.4	-67.5	0.4	-67.5	0.4	-67.5	0.4	<i>MLO</i>
7951.19236	2951	45	-71.0	1.3	-68.2	1.4	-69.6	1.1	-70.6	0.8	-60.7	1.9	<i>AAVSO-V-2</i>
7988.74625	2989	187	-68.3	4.7	-75.8	5.6	-72.1	4.3	-71.9	2.4	-62.6	4.3	<i>ASAS-SN-4</i>
8076.66821	3076	71	-75.1	2.9	-77.2	2.8	-76.2	2.3	-70.6	0.9	-64.0	1.9	<i>AAVSO-V-3</i>
8225.95586	3226	47	-81.7	1.1	-82.0	1.0	-81.8	0.9	-83.1	0.5	-67.9	0.9	<i>AAVSO-V-4</i>
8338.60728	3338	36	-88.4	0.6	-86.3	0.6	-87.3	0.5	-87.0	0.4	-83.1	0.5	<i>AAVSO-V-5</i>
8354.63426	3354	150	-90.3	2.0	-90.6	2.0	-90.4	1.7	-85.7	0.9	-83.1	2.0	<i>AAVSO-I-1</i>

¹All input time series are transformed to the BJD timebase.²See Appendix A for the details of the preparation of each data segment.

Notes: $T_{\text{obs}}(1)$: observed moment of the primary minimum minus 2450000.0, derived from a 4-th order Fourier fit; T_{mid} : center of the observational time span minus 2455000.0; ΔT : half range of the observational time span; OC# : various observed minus calculated moments of minima, as described in Sect. 2; eOC# : 1σ statistical error of OC#. The calculated epochs of the primary minima are given by $C = 2454953.949183 + E \times 0.4579515$, where E is the closest integer cycle number for the given primary minimum. All O-C values resulted from the analysis presented in this paper, except for the values of Vulcan and MLO. For these we adopted the values by Socia et al. (2018). See Sect. 3 and Table 2 for the template selection in computing OC4 and OC5.

that former works by Molnar et al. (2017) and Socia et al. (2018) did not use the WASP segment near HJD - 2455000.0 = -2000, the HATNet, the ASAS-SN the AAVSO and the WISE data (but they used their own observations). The horizontal coordinate of each subset corresponds to the center of the time span of the given set. The horizontal bars are the half ranges of these time spans.

We see that the Vulcan observations (second point from the left) and the HATNet and WASP data clearly breaks the exponential trend fitting based on data gathered after JD= 2455000.0³. Furthermore, assuming a simple linear period

change for the approximation of the overall parabolic trend, leads also to an unsatisfactory fit (magenta line in Fig. 4). The smooth, non-monotonic deviations from these simple representations indicate that the observed O-C values require a somewhat more involved modeling.

3. Decomposition of the O-C variation

Due to the limited number of data points, we aim for a modeling that is parsimonious with respect of the number of parameters fitted, and, at the same time, physically sound. This leads to the

³ In supporting this trend, there was also the point from the NSVS archive. However, as pointed out by Socia et al. (2018), this suffered

from an MJD/HJD ambiguity in the work of Molnar et al. (2017), that yielded the apparent confirmation of the exponential trend.

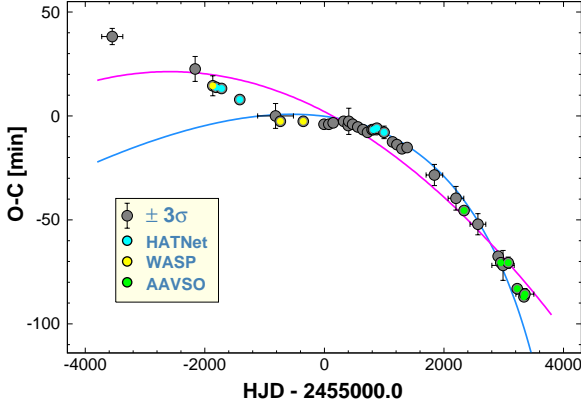


Fig. 4. Observed minus calculated moments of the primary minima for KIC 9832227. We used the template fit method yielding the OC4 values as described in Sect. 2. The reference period and epoch of the primary eclipse are the same used by Socia et al. (2018), i.e., $P = 0.4579515$ d, $EPOCH = 2454953.949183$ BJD. Light blue line shows the exponential model of Molnar et al. (2017) reaching singularity in 2022.2 (i.e., at $HJD - 2455000.0 = 4651$). Assuming only a linear period decrease, we get the best fitting parabola shown by the magenta line. Data associated with certain surveys are highlighted. See Table 1 for the full dataset.

obvious choice of decomposing the observed O-C values into components of a linear period decrease and a periodic variation, modelled simply with a sine function of arbitrary amplitude and phase

$$O - C = c_1 + c_2 t + c_3 t^2 + c_4 \sin\left(\frac{2\pi t}{P_2}\right) + c_5 \cos\left(\frac{2\pi t}{P_2}\right), \quad (2)$$

where O-C is the observed timing difference in [min], $t = HJD - 2455000.0$ and P_2 is the period of the sinusoidal component. The other possibility would be to continue with higher order polynomial representation. To test briefly the goodness of fit for the pure polynomial approximation, we used the OC4 data (see Table 1 – the observed moments of minima have been derived with the aid of template *Kepler-4*). Here, and throughout the paper, Eq. 2 is fitted by simple Least Squares with equal weights. For the fourth order polynomial fit the unbiased RMS of the fit was 2.83 min, exceeding significantly the fitting RMS of 1.38 min of the pol+sin model. We may get similar RMS of 1.46 min with the pure polynomial fit, if we increase the order by one, but then the fit suggests a steep downward trend for dates less than -3600 . Further increase of the polynomial order leads to overshoot in the empty part of the dataset, between -3600 and -2100 . We see that there is a preference toward the data representation indicated by Eq. 2.

To determine the best period for the sinusoidal component, we scanned the period in the [4000, 8000] d interval and searched for the lowest residual scatter given by the Least Squares fit of Eq. 2. With the best period found, we followed the same type of simple Monte Carlo method to estimate the error of the period, as described in Sect. 2 for the calculation of the errors of the O-C values. Figure 5 shows the run of RMS for the finally accepted method, using full phase-folded light curve fit by employing the set *Kepler-4* as the template. Comparison with the other methods and templates is given in Table 2. We see that the full-phase template fit performs well, with some dependence

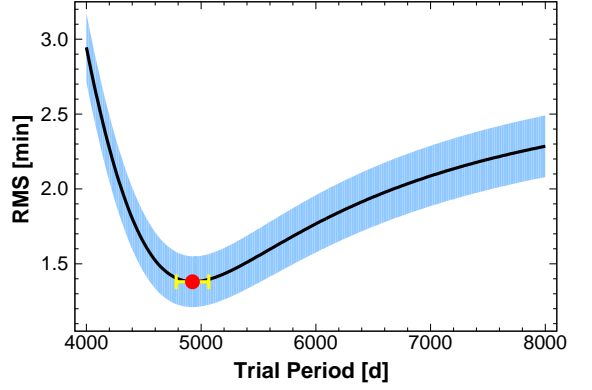


Fig. 5. Period scan of the O-C data obtained by the template fit method (see column OC4 of Table 1). Equation 2 is used to find the minimum RMS of the residuals (black line). The 1σ ranges of the residuals of the simple Monte Carlo simulations are shown by the shaded area. The optimum period and its 1σ error from the above simulations is shown by the red dot and its error bar.

on the template used. Based on these tests, we set the long-term modulation period P_2 equal to (4925 ± 142) d.

Table 2. Modulation periods derived by various methods.

OC#	P_2 (d)	σ_{fit} (min)	Template
1	5427 ± 266	1.684	–
2	5045 ± 492	3.678	–
3	5206 ± 243	1.852	–
4	4965 ± 185	1.633	AAVSO-V-4
	4925 ± 142	1.380	<i>Kepler-4</i>
	4985 ± 169	1.537	AAVSO-V-1
5	4683 ± 276	3.261	AAVSO-V-4
	5990 ± 747	2.689	<i>Kepler-4</i>
	4965 ± 320	3.019	AAVSO-V-1

Notes: The type of the fit employed on the light curves is given in the first column and defined in Sect. 2 (the first three refer to Fourier-based O-C values, the 4-th and 5-th to template-based values with the template indicated in the last column). Equation 2 has been fitted by Least Squares to derive σ_{fit} for the best modulation period. The 1σ errors of the periods were calculated with the aid of a simple Monte Carlo method. The best solution is highlighted.

With the period known, we can decompose the data into a quadratic and a periodic part. The result is shown in Fig. 6. It seems that this simple model fits the data near the noise level expected from the physical jitter of the minima due to stellar activity (Socia et al. 2018) and from the overall statistical error due to observational noise.

The regression parameters and their standard errors are listed in Table 3. The errors are 1σ standard deviations and derived directly from the inverse of the normal matrix. The error of the amplitude of the periodic component results from random simulations assuming independent Gaussian errors with standard deviations given on c_4 and c_5 from the normal matrix. Both Fig. 6 and the errors of the physically interesting quantities (period change $P\dot{\text{dot}}$ and amplitude of the periodic component $Ampl$) together with the low residual scatter indicate that the chosen mathematical representation is quite suitable for the description of the available data. For a sanity check of the solution above,

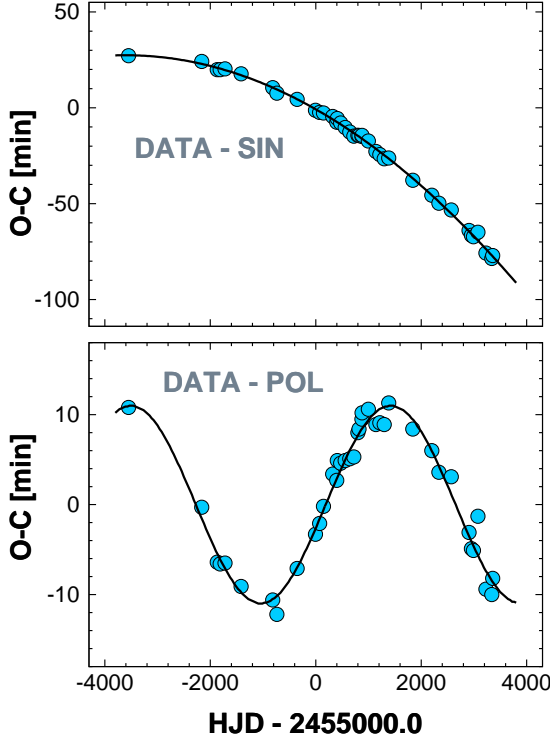


Fig. 6. Result of the joint fit of a second order polynomial and a single sinusoidal to the data shown Fig. 4. The data plotted in the upper panel are free from the sinusoidal, whereas those shown in the lower panel from the polynomial component. See Table 3 for the regression coefficients of these components.

Table 3. Parameters of the polynomial+sinusoidal fit.

Coeff	Value	Error	
c_1	$-0.76257 \times 10^{+0}$	$0.38377 \times 10^{+0}$	
c_2	-0.15618×10^{-1}	0.14628×10^{-3}	
c_3	-0.21632×10^{-5}	0.09212×10^{-6}	
c_4	$0.10659 \times 10^{+2}$	$0.35694 \times 10^{+0}$	
c_5	$-0.26196 \times 10^{+1}$	$0.47482 \times 10^{+0}$	
Associated quantities			
Name	Unit	Value	Error
P_2	[d]	4925	142
RMS	[min]	1.380	0.169
$Pdot$	[d/yr]	-1.097×10^{-6}	0.047×10^{-6}
$Ampl$	[min]	10.976	0.365

Notes: For the meaning of the regression coefficients $\{c_i\}$ see Eq. 2. Errors on $\{c_i\}$ do not include the contribution from the period.

in Appendix B we present the solution obtained by the Markov Chain Monte Carlo (MCMC) method.

In spite of the good fit to the observations, the predictive power of the derived polynomial+sinusoidal model is not very high. For a fixed period of the sinusoidal component one can give an estimate on the variance of the predicted O-C values for arbitrary moments by using the inverse of the normal matrix of the linear regression of Eq. 2

$$\sigma_{\text{pred}}^2(i) = \sigma_{\text{fit}}^2 \sum_{j=1}^5 \sum_{k=1}^5 G(j, k) x(j, i) x(k, i), \quad (3)$$

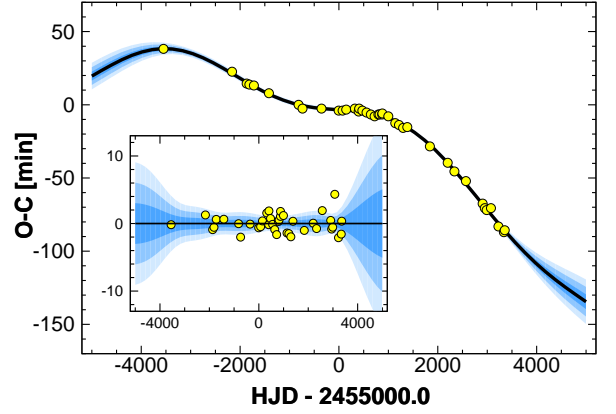


Fig. 7. Polynomial+sinusoidal fit (thick black line) of the observed O-C values (yellow dots, OC4 of Table 1). In the order of lighter shading, the blue regions show the 1, 2 and 3 sigma limits of the predicted O-C ranges, assuming errors in all estimated parameters, including P_2 , the period of the long-term variation. The inset shows the deviation from the best fit to the currently available data.

where σ_{fit} is the unbiased standard deviation of the residual of the regression, $\{G(j, k)\}$ is the inverse of the normal matrix, and $\{x(j, i)\}$ is the set of vectors associated with the j -th regression coefficient c_j (see Eq. 2) at moment t_i . Although the above formula is exact, it lacks accounting for the error introduced by the period P_2 . To consider the contribution of the period estimation, we need to perform a Monte Carlo simulation. Here we use the synthetic data obtained by the fit to the original input time series with the best period. We add observational noise (Gaussian, with the standard deviation given by σ_{fit}) and then fit the data by Eq. 2, where P_2 is also perturbed with a Gaussian error of $\sigma = 142$ (see Table 3). We repeat this process 500 times and arrive to the point-by-point standard deviations of the realization-dependent predicted O-C values. Figure 7 shows the resulting regions visited by the realizations, scaled by σ_{pred} . We note that using Eq. 3 (i.e., neglecting the effect of the P_2 ambiguity), we get a somewhat more restricted prediction space, with a 3σ limit corresponding to the 2σ limit of the result shown. In any case, if the model is correct, in the following 3–4 years the periodic component will pass the minimum and starts to rise by a few minutes, that could be verified rather easily even by sporadic observations.

4. Physical interpretation

First we discuss the possible physical causes giving rise to the periodic component of the O-C variation. There could be three possible causes of this type of variation: (i) change in the stellar structure due to stellar magnetic cycles (the so-called Applegate-effect – see Applegate 1992); (ii) apsidal motion mainly due to the finite size and non-spherical shape of the components (e.g., Mazeh 2008); (iii) light-time effect, due to an external perturber (e.g., Wolf 2014).

For a brief check of possibility (i) we follow Almeida et al. (2019) and use the empirical studies of Oláh et al. (2009), Savanov (2012) and Vida et al. (2013, 2014) to see if our target follows the relation between the rotation frequency and the magnetic cycle length. We make the obviously non-stringent assumption that the orbital period is a good proxy of the rotation period. The result is shown in Fig. 8. Because our target

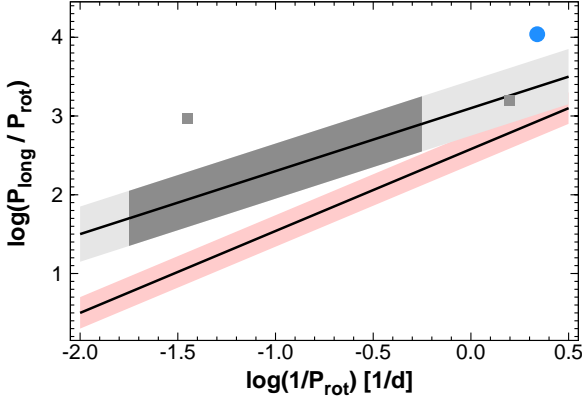


Fig. 8. Position of KIC 9832227 (light blue dot) on the schematic diagram relating the rotation frequency to the ratio of the period of the long-term cyclic luminosity variation due to stellar activity to the rotation period. The shaded area cover the data points shown by Almeida et al. (2019), based on the studies of Vida et al. (2013, 2014), Oláh et al. (2009), and Savanov (2012). Pink shade is used for red dwarfs, dark gray for other stars, with the extension to non-populated regions (light gray). Isolated small gray squares indicate objects distinct from the bulk of the sample.

has rather small error bar even on the longer period – yielding $\sigma(\log(P_{\text{long}}/P_{\text{rot}})) \sim 0.013$ – the outlier status of this object is quite likely, assuming that the observed trend continues also in the currently poorly explored parameter regime.

Possibility (ii) may occur due to the slow drift of the apsis line in systems with eccentric orbits. One of the characteristics of this phenomenon is the anticorrelation of the timings of the primary and secondary minima (e.g., Wolf, Zejda & de Villiers 2008). For our target, this explanation is also unlikely. First, the eccentricity must be very small, as suggested by the good fit of the radial velocity data with the assumption of zero eccentricity (see Molnar et al. 2017). Second, the difference between the primary and secondary O-C values (see Table 1) also supports the assumption of near zero eccentricity. Indeed, leaving out the secondary eclipse outliers *WISE-W12* and *HAT-5*, the average difference ($\Delta T = T_2 - T_1 - P_{\text{orb}}/2$) is -2.0 min with a standard deviation of 2.7 min for the remaining 37 points. This implies – see, e.g., Winn 2010 – $e \cos \omega = \frac{\pi \Delta T}{2P_{\text{orb}}} = 0.005 \pm 0.001$, where the error has been estimated from the error of the average ΔT . Third, the period of the sinusoidal component of the O-C variation of our target is relatively short, and therefore, not too common among objects showing apsidal motion (see Hong et al. 2016 and Zasche et al. 2018).

Possibility (iii) implies that the system is a hierarchical triplet, with an outer component on a 4925 d orbit. The mass function can be estimated from the amplitude of the sinusoidal component of the total O-C variation. With the assumption of zero eccentricity, this yields: $M_3 \geq (0.38 \pm 0.02) M_{\odot}$, where the error is the standard deviation of the values obtained by including the Gaussian errors of all constituent parameters. We recall that this mass (although it is a lower limit) is still allowed by the test performed on the composite spectral broadening function by Molnar et al. (2017). They suggest an upper limit of $0.5 M_{\odot}$ for any possible third component, assuming that it is a main sequence star.

Although it is not expected that the third star with its low luminosity (implied by its mass) will give any appreciable con-

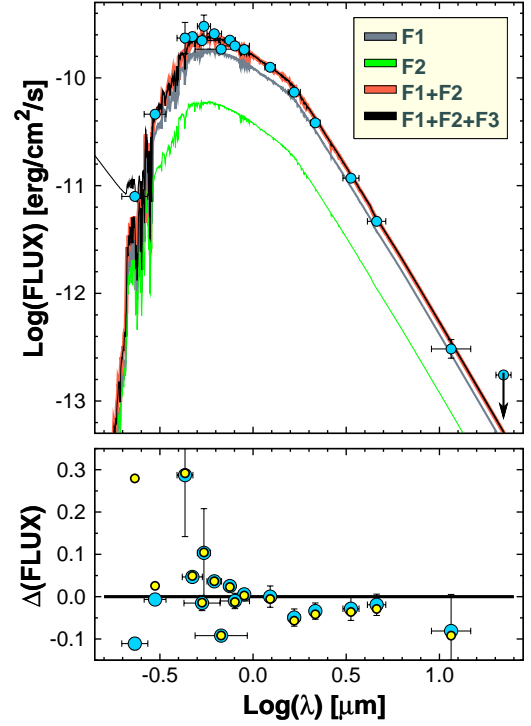


Fig. 9. Comparison of the observed and theoretical SEDs for KIC 9832227. Dots denote observed values, with 3σ vertical error bars, and equivalent waveband widths (horizontal bars). The inset shows the various theoretical SEDs: F1 - primary only, F2 - secondary only, F1+F2 - binary only, F1+F2+F3 - binary, with the hypothetical 3rd component – K/M dwarf or white dwarf (black lines, differ only in the UV). The lower panel shows the residual in respect of the three-component solution: blue dots - white dwarf, yellow dots: K/M dwarf for the 3rd component. The stellar atmosphere models of Castelli, Gratton & Kurucz (1997) and Koester (2010) are used (see text and Appendix C for more details).

tribution to the total spectral energy distribution (SED) of the system, it is still useful to check the actual values and explore the effect of components different from a main sequence star. We gathered 18 wide-band color values from the near ultraviolet to infrared regime. After converting all magnitudes to the Vega system, we compared these values by the theoretical SEDs obtained from various stellar atmosphere models (we refer to Appendix C for additional details on the data and the models). The final SED values are plotted in Fig. 9.

Assuming that the third component is a main sequence star (a late K dwarf or an early M dwarf) we set its radius equal to $0.4 R_{\odot}$. For the binary we used the parameters of Molnar et al. (2017) and the Gaia distance (585 ± 10 pc) to derive the observable fluxes from the stellar atmosphere model fluxes. As it is shown in Fig. 9, with the main sequence assumption we cannot get any additional support for the existence of the third component. Furthermore, we note that the analysis of the NIR spectra made by the NASA Infra-Red Telescope Facility by Pavlenko et al. (2018) also did not show any obvious sign of the presence of a third component.

On the other hand, we see that the Galex NUV flux at the far left is significantly above the model flux. This observation led us to test the possibility of another third body scenario, by assuming that it is a relatively low-mass white dwarf (WD). We

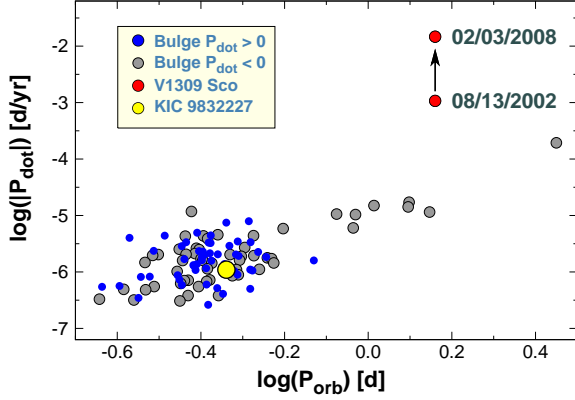


Fig. 10. Comparison of the size of the observed period changes of various groups of binaries. The verified pre-nova V1309 Sco stands out with its huge rate and its change within six years of observing time span. On the other hand, KIC 9832227 sits right in the middle of the binaries showing significant, but relatively low, negative period change in the Galactic Bulge sample of Pietrukowicz et al. (2017). For comparison, we also plot the stars from the above survey, showing period increase.

see that adding the flux of a $T_{\text{eff}} = 30000$ K, $R = 0.016 R_{\odot}$ WD almost cures the discrepant position of the NUV flux, but (obviously) leaves the overall fine match at all other wavelengths. Nevertheless, the scatter at the peak SED regime is still somewhat high, likely because of the larger observational errors of some of the fluxes – the flux variations due to eclipses are rather small, and some fluxes result from averaging several observations spread through many orbital periods. For instance, the outlier status of the Gaia G-band is hard to understand at this moment, because it is surely not due to some “single measurement / bad phase” effect. In addition to the scatter, an upward trend toward shorter wavelength near the peak flux is also observable. This is sign of the overestimation of the reddening. Indeed, as discussed in Appendix C, the reddening value of $E(B - V) = 0.082$ based on the map of Schlafly & Finkbeiner (2011) is more than a factor of two higher than the one derived by Molnar et al. (2017) from the combination of spectroscopic and photometric data. With $E(B - V) = 0.03$ we can eliminate the trend and considerably lower the likelihood of the WD scenario, but (obviously) we cannot cure the scatter around the maximum flux.

Concerning the monotonic component of the total period variation, it is interesting to compare the rate of period change with those observed in other binaries. As a basis of comparison, we selected the recent analysis of 22500 binaries in the Galactic Bulge by Pietrukowicz et al. (2017). Figure 10 shows that the rate of period change of KIC 9832227 is quite similar to most of the stars analyzed in the above work. Indeed, V1309 Sco, the only verified nova precursor (Tyndea et al. 2011) clearly stands out with its dramatic period decrease from the other, ‘normal’ binaries. Although there is an excess of systems with higher negative period change, the nearly equal number of systems with positive and negative period changes (52 and 56, respectively) indicates that the cause of most of the period changes lies in some temporal (long-term) variation rather than an inward spiraling of the components. One possibility is the presence of distant perturbers with substantially longer period than the time span of the data. In the analysis performed by Pietrukowicz et al. (2017), the time base extends from 1997 to 2015 – and, in some cases from 1992, depending on the availability of data from the var-

ious OGLE phases. Even though this 20–25 yr time span is quite remarkable, there are several examples on systems with tertiary components of even longer periods (e.g., Sarotsakulchai et al. 2019 and Tokovinin 2014 for a review). It is also worthwhile to recall that Pietrukowicz et al. (2017) identified also 35 binaries with cyclic O-C variations. The high number of cyclic period changers is further supported by the current survey of the same area by Hajdu et al. (2019), using all available data from the OGLE-IV archive. From the 80000 systems examined, they found 992 with cyclic O-C variations. We conclude that in the specific case of KIC 9832227 the total time span of the data used in this investigation is ~ 19 years, which leaves still enough room for the 4th-body interpretation of the apparent linear period change. At the same time, continuation of the monotonic variation of the period is also a possibility. This may come from various sources, such as mass transfer within the W UMa components, angular momentum loss due to magnetic wind – e.g., Yang & Liu (2003) and Toonen et al. (2016). The complex nature of these processes do not allow a more detailed study of these possibilities within the limitation of this work.

5. Conclusions

The work by Socia et al. (2018) on the negation of the nova candidate status of KIC 9832227 stimulated our deeper investigation of this W UMa-type binary system. Because the conclusion of Socia et al. (2018) rests mainly on the misidentification of a single early epoch, we thought that the period variation should be further investigated by using additional data available from various ground- and space-based instruments. Thanks to the wide field survey HATNet and to the renewed analysis of the WASP survey, we successfully filled out a crucial early period of the O-C variation. In addition to the already utilized public domain data by Molnar et al. (2017) and Socia et al. (2018) we also found extremely useful data from the supernova survey ASAS-SN, AAVSO and from the WISE satellite. The 39 epochs were accurate enough to clearly decompose the period variation into a linear and a sinusoidal parts. We found that the linear rate of change is equal to $(-1.097 \pm 0.047) \times 10^{-6}$ d/yr. This value fits in the overall rate observed in many binary systems. The period and the amplitude of the sinusoidal components are equal to (4925 ± 142) d and (10.98 ± 0.37) min. We found that the most plausible explanation for the source of this variation is the light-time effect of an outer perturber. The estimated lower limit of the mass of the outer companion is $(0.38 \pm 0.02) M_{\odot}$. This value – assuming that the third component is a main sequence star – is below the upper mass limit allowed by the non-detection of the corresponding feature in the broadening function analysis of Molnar et al. (2017). With the significant deviation of the GALEX NUV point from the composite SED constructed under the assumption of a main sequence tertiary, we also tested the replacement of this component with a white dwarf. We found a better fit, but the contribution of the white dwarf component induces a large UV excess at shorter wavelengths. Currently, there are no data available at these short wavelengths, but future observations might easily confirm or negate the viability of the white dwarf scenario. A further ambiguity in the white dwarf hypothesis is the poorly known value of the reddening. By using $E(B - V) = 0.03$ – i.e., more than a factor of two lower value than the one employed in this paper – decreases the probability of a white dwarf companion considerably.

Acknowledgements. We thank Sebastian Otero at AAVSO for answering our questions on various aspects of the data accessed. We are grateful to the observers as listed in Appendix A of this paper for their valuable contribution via

the AAVSO database. We acknowledge the improvement in the model fit by following the suggestion of the referee of using uniform timebase (i.e., BJD) for all data. Thanks are due also to Yakiv Pavlenko, for the correspondence on the analysis of the NIR spectra. This research has made use of the International Variable Star Index (VSX) database, operated at AAVSO, Cambridge, Massachusetts, USA. This paper includes data collected by the Kepler mission. Funding for the Kepler mission is provided by the NASA Science Mission directorate. This publication makes use of data products from the Wide-field Infrared Survey Explorer, which is a joint project of the University of California, Los Angeles, and the Jet Propulsion Laboratory/California Institute of Technology, funded by the National Aeronautics and Space Administration. The NSVS data have been downloaded from the site of SkyDOT, operated by the University of California for the National Nuclear Security Administration of the US Department of Energy. This research has made use of the VizieR catalogue access tool, CDS, Strasbourg, France (DOI: 10.26093/cds/vizieR). Supports from the National Research, Development and Innovation Office (grants K 129249 and NN 129075) are acknowledged. Data presented in this paper are based on observations obtained by the HAT station at the Submillimeter Array of SAO, and the HAT station at the Fred Lawrence Whipple Observatory of SAO. HATNet observations have been funded by NASA grants NNG04GN74G and NNX13AJ15G.

References

- Abbott, B. P., Abbott, R., Abbott, T. D. et al. 2016, *Phys. Rev. Lett.*, 116, 061102
- Almeida, L. A., de Almeida, L., Damineli, A. et al. 2019 *AJ*, 157, 150
- Apellaniz, J. M. & Gonzalez, M. P. 2018, *A&A*, 616, L7
- Applegate, J. H. 1992, *ApJ*, 385, 621
- Bakos, G.; Noyes, R. W.; Kovács, G., et al. 2004, *PASP*, 116, 266
- Bakos, G. Á., Torres, G., Pál, A., et al. 2010, *ApJ*, 710, 1724
- Borucki, W. J., Caldwell D., Koch D. G. et al. 2001, *PASP*, 113, 439
- Borucki, W. J., Koch, D., Basri, G. et al. 2010, *Science*, 327, 977
- Bovy, J., Rix, H.-W., Green, G. M. et al. 2016, *ApJ*, 818, 130
- Castelli, F., Gratton, R. G. & Kurucz, R. L., 1997, *A&A*, 318, 841
- Davenport, J. R. A., Ivezić, Z., Becker, A. C. et al. 2014, *MNRAS*, 440, 3430
- Ferreira, T., Saito, R. K., Minniti, D. et al. 2019, *MNRAS*, 486, 1220
- Frei, Zs. & Gunn, J. E. 1994, *AJ*, 108, 1476
- Hajdu, T., Borkovits, T., Forgács-Dajka, E. et al. 2019, *MNRAS*, 485, 2562
- Hong, K., Lee, J. W., Seung-Lee Kim, S.-L. et al. 2016, *MNRAS*, 460, 650
- Kirk, B., Kyle Conroy, K., Prsa, A. et al. 2016, *AJ*, 151, 68
- Kochanek, C. S., Shappee, B. J., Stanek, K. Z. et al. 2017, *PASP* 129, 104502
- Koester, D. 2010, *Memorie della Societa Astronomica Italiana*, 81, 921
- Kovacs, G., Bakos, G., Noyes, R. W. 2005, *MNRAS*, 356, 557
- Kovacs, G. 2018, *A&A*, 614, L4
- Kuncarayakti, H. 2016, *Journal of Physics: Conference Series*, 728, 072019
- Law, N. M., Kulkarni, S. R., Dekany, R. G. et al. 2009, *PASP*, 121, 1395
- Liu, T., Janes, K. A., 1990, *ApJ*, 354, 273
- Mason, E., Diaz, M., Williams, R. E. 2010, *A&A*, 516, A108
- Mazeh, T. 2008, *EAS Publications Series* 29, 1
- McCall, M. L. 2004, *AJ*, 128, 2144
- Molnar L. A., van Noord D. M., Kinemuchi K. et al. 2017, *ApJ*, 840, 1
- Nakano, S., Nishiyama, K. & Kabashima, F. 2008, *IAU Circ. No.* 8972
- Oláh, K., Kolláth, Z., Granzer, T., et al. 2009, *A&A*, 501, 703
- Pastorello, A., Mason, E., Taubenberger, S. et al., 2019, *A&A* (submitted), arXiv:1906.00812
- Pavlenko, Ya. V., Evans, A., Banerjee, D. P. K. et al. 2018, *A&A*, 615, 120
- Pejcha, O., Metzger, B. D., Tyles, J. G. et al. 2017, *ApJ*, 850, 59
- Pietrukowicz P., Soszyński I., Udalski A. et al. 2017, *AcA*, 67, 115
- Pollacco, D. L., Skillen, I., Collier Cameron, A., et al. 2006, *PASP*, 118, 1407
- Podsiadlowski, Ph., Joss, P. C. & Hsu, J. J. L. et al. 1992, *ApJ*, 391, 246
- Pojmanski, G., Pilecki, B. & Szczygiel, D. 2005, *AcA*, 55, 275
- Rau, A., Kulkarni, S. R., Law, N. M. et al. 2009, *PASP*, 121, 1334
- Romero, A. D., Kepler, S. O., Joyce, S. R. G. et al. 2019, *MNRAS*, 484, 2711
- Sanders, J. L. & Das, P. 2018, *MNRAS*, 481, 4093
- Sarotsakulchai, T., Qian, S.-B., Soonthornthum, B. et al. 2019, *PASJ*, 71, 81
- Savanov, I. S. 2012, *ARep*, 56, 716
- Schlaflly, E. F. & Finkbeiner, D. P. 2011, *ApJ*, 737, 103
- Shappee, B. J., Prieto, J. L., Grupe, D. et al. 2014, *ApJ*, 788, 48
- Smith, J. C., Stumpe, M. C., Van Cleve, J. E. et al. 2012, *PASP*, 124, 1000
- Socia, Q. J., Welsh, W. F., Short, D. R. et al. 2018, *ApJ*, 864, L32
- Tamuz, O., Mazeh, T., & Zucker, S. 2005, *MNRAS*, 356, 1466
- Ter Braak, C. J. F. 2006, *Stat. and Comp.*, 16, No. 3, 239
- Tokovinin, A. 2014, *AJ*, 147, 87
- Toonen, S., Hamers, A., Portegies, Z. S. 2016, *Computational Astrophysics and Cosmology*, Volume 3, Issue 1, article id. 6, 36 pp
- Truran, J. W. & Cameron, A. G. W., 1971, *Ap&SS*, 14, 179
- Tylenda R., Hajduk M., Kamiński T. et al. 2011, *A&A*, 528, A114
- Vida, K., Kriskovics, L., & Oláh, K. 2013, *AN*, 334, 972
- Vida, K., Oláh, K., & Szabó, R. 2014, *MNRAS*, 441, 2744
- Wang, S. & Chen, X. 2019, *ApJ*, 877, 116
- Winn, J. N. 2010, arXiv:1001.2010v5
- Wolf, M. 2014, *CoSca*, 43, 493
- Wolf, M., Zejda, M. & de Villiers, S. N. 2008, *MNRAS*, 388, 1836
- Woźniak, P. R., Vestrand, W. T., Akerlof, C. W. et al. 2004, *AJ*, 127, 2436
- Wright, E. L., Eisenhardt, P. R. M., Mainzer, A. K. et al. 2010, *AJ*, 140, 1868
- Yang, Y. & Liu, Q. 2003, *PASP*, 115, 748
- Yuan, H. B., Liu, X. W. & Xiang, M. S. 2013, *MNRAS*, 430, 2188
- Zasche, P., Wolf, M., Uhlar, R., et al. 2018, *A&A*, 619, 85

Appendix A: Data sources and data handling

Here we describe some relevant pieces of information concerning the data used in the O-C analysis as displayed in Table 1. First we note that the values for the Vulcan and MLO data have been taken from Socia et al. (2018) (as a result, all OC values are the same for these items). In the case of the AAVSO data, we used only *V* and *I* observations, because other colors did not have proper phase coverage. The web sites and the appropriate journal references for the data sources are as follows.

- AAVSO: <https://www.aavso.org/vsx/>
- ASAS: <http://www.astrouw.edu.pl/asas/>
 - Pojmanski, Pilecki & Szczygiel (2005) and references therein
- ASAS-SN: <https://asas-sn.osu.edu/>
 - Shappee et al. (2014) and Kochanek et al. (2017)
- Kepler: <http://keplerebs.villanova.edu/>
 - Borucki et al. (2010) and Kirk et al. (2016)
- NSVS: <https://skydot.lanl.gov/nsvs/nsvs.php>
 - Woźniak et al. (2004)
- WASP: <https://wasp.cerit-sc.cz/form>
 - Pollacco et al. (2006)
- WISE: <https://irsa.ipac.caltech.edu/cgi-bin/Gator/np>

The HATNet data are publicly accessible from the website <https://data.hatsurveys.org>. The data used in this paper are accessible through the CDS link given in Sect. 2. These data result from an early reduction and therefore might be slightly different from the data included in the full public HAT archive. Nevertheless, the possible differences are expected to have only small effects on the O-C values.

Following the notation of Table 1, the notes below are relevant from the point of the analysis presented in this paper (see also some related notes in Sect. 2).

AAVSO-V-1 – AAVSO-V-5: Because the data have been gathered from different observers with different instruments, they are often not on the same zero point. Also, not all data are of the same quality. If necessary, we adjusted the quality requirement to the goal of segmental sampling by omitting entirely observations owned by a given observer. By using the observer assignment code of AAVSO data site, we broke down the *V* data in the following way. AAVSO-V-1: observer PVEA (*Velimir Popov*); AAVSO-V-2: observers SAH (Gerard Samolyk), RIZ (*John Ritzel*) and TRE (*Ray Tomlin*) with a zero point shift applied only to SAH; AAVSO-V-3: observers CDSA (*David Conner*), HJW (*John Hall*), DUBF (*Franky Dubois*) and TRE, ZP(CDSA)=+0.037, and all other zero point shifts are zero; AAVSO-V-4: observers KTU (*Timo Kantola*), HJW and TRE and ZP(KTU)= −0.04; ZP(HJW)= −0.025; AAVSO-V-5: observers TRE, SAH, SNE (*Neil Simmons*) and DUBF, with ZP(SAH)= +0.019, and all other zero point shifts are zero. AAVSO-I-1: The data from DUBF and TRE are used, with ZP(DUBF)= −0.0092.

ASAS-IV: Because the data suffer from relative high observational noise, the observations made in *I* and *V* colors have been merged with a zero point shift of +0.717 for the *I* data. We selected “grade A” data from the *V* observations and averaged the magnitudes in columns #2 to #5, corresponding to different aperture sizes. For the *I* data the “grade A” selection resulted only five data points. Therefore, we used all data points and averaged only columns #4 and #5.

ASAS-SN-1 – ASAS-SN-4: The data quality and the number of data points allowed us to separate the full dataset into four segments.

HAT-1 – HAT-5: To avoid possible signal suppression when the data are corrected for instrumental systematics but they are not reconstructed by using the full (signal+systematics) model, we used the magnitudes derived from an ensemble photometry, based on aperture fluxes. Because of the large field of view, the ensemble value of the stars observed during each exposure depends on the chip position (e.g., vignetting causes large changes in the stellar fluxes). From the three aperture sizes we selected the one that resulted the smallest scatter of the folded light curve. Although dataset #4 is already compact in its entirety, it has been divided into two parts, because of the large number of data points allows us to do so, and thereby effects of short term light curve changes can be assessed.

Kepler-1 – Kepler-15: The data quality and the number of data points allowed us to separate the full dataset into 15 segments with ~ 3500 data points in each segment. We avoided including different Quarters in the same data segment, if zero point differences were obvious. Similarly to the HAT data, the simple aperture flux (column #3) is used to avoid possible signal degradation when the data are corrected for instrumental systematics and not a full signal model is used.

NSVS-12: We employed the data acquired by the two cameras observing the field that hosts KIC 9832227. As in other cases, the moments of observations have been transformed to BJD (in this particular case, from MJD). A zero point correction of 0.060 mag is also applied to the dataset acquired by one of the cameras.

WASP-1, WASP-3, WASP-4: Unfortunately, we had to leave out *WASP-2*, because of the bad phase coverage of the data points for this dataset between HJD 2453901.662 and 2453952.427.

WISE-W12: This is a merged set of the data gathered in the W1 and W2 filters. The data have been taken in two campaigns, separated by a gap of half a year. There is a zero point shift of ~ 0.03 mag between the two segments. A closer examination also shows that the data from the two bands also have zero point differences of the order of ~ 0.01 mag, that depends also on which of the above two campaigns is considered. By performing these campaign- and filter-dependent shifts, we ended up with a time series containing 116 items. In spite of the above adjustments, the data still show significant scatter of 0.028 mag around a 4-th order Fourier fit. Nevertheless, the accuracy of the O-C value is still acceptable for our purpose.

Appendix B: The MCMC solution

In finding the best-fit solution for Eq. 2 to the O-C data of Table 1 (labelled by OC4), we performed a Differential Evolution Markov Chain Monte Carlo (DEMCMC) analysis following Ter Braak (2006). We assumed uniform priors on all of the parameters given in Eq. 2. Additionally we introduced a parameter to account for excess scatter in the O-C values above the estimated uncertainties. This scatter was added in quadrature to

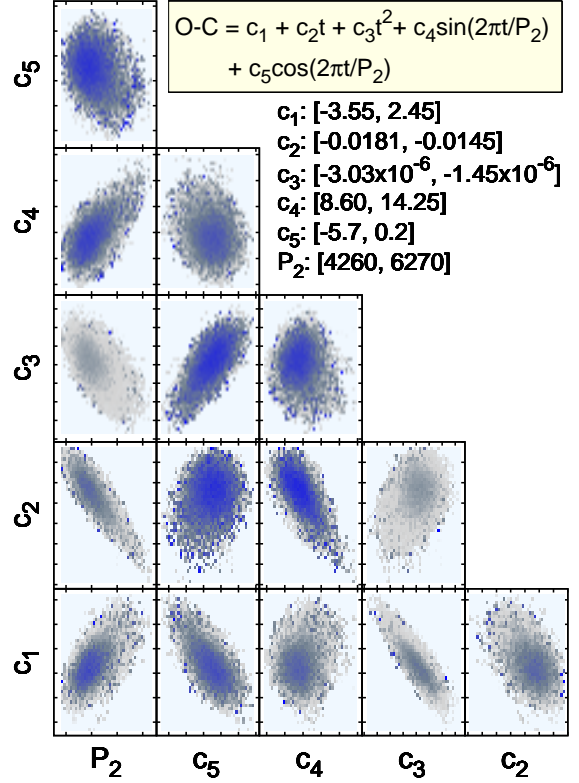


Fig. B.1. Diagnostic diagram based on the MCMC solution of the fit of the polynomial+sinusoidal model (see inset) of the observed O-C values (see Table 1). Coloring goes with the χ^2 values: the blue ones have the smallest χ^2 , whereas the gray dots with decreasing intensity are associated with the less probable solutions. To avoid crowdedness, we list the parameter ranges of the plots within the figure.

all of the listed errors, and was allowed to vary in the analysis using a uniform logarithmic prior.

The resulting parameter-parameter plots are shown in Fig. B.1. In most cases the cross-correlation effect is not substantial, at least in the close neighborhood of the high-density / low- χ^2 regimes that determine the most probable solution. We collected the final parameters with their 1σ errors in Table B.1. In comparing the solution derived from the standard Least Squares fit (see Table 3), we see a good agreement for the parameter values. However, the MCMC errors are larger. This is because the errors include the effect of the various choices of all other parameters, whereas in our Least Squares solution the period was fixed to its optimum value.

Appendix C: SED’s constituents

The magnitudes measured for KIC 9832227 have been gathered from the VizieR⁴ site. All magnitudes have been transformed to the Vega system, by using the filter zero points as given at the Spanish Visual Observatory site⁵. To derive dereddened magnitudes, we accepted the reddening given by the map of Schlafly & Finkbeiner (2011) and accessible at the NASA/IPAC Infrared

⁴ <https://vizier.u-strasbg.fr/viz-bin/VizieR>

⁵ <http://svo2.cab.inta-csic.es/theory/fps/>

Table B.1. Best-fit parameters of the polynomial+sinusoidal model by MCMC.

Coeff	Value	Error	
c_1	$-0.8765 \times 10^{+0}$	$0.5456 \times 10^{+0}$	
c_2	-0.1567×10^{-1}	0.3362×10^{-3}	
c_3	-0.2160×10^{-5}	0.1424×10^{-6}	
c_4	$0.1071 \times 10^{+2}$	$0.4788 \times 10^{+0}$	
c_5	$-0.2539 \times 10^{+1}$	$0.5617 \times 10^{+0}$	
Associated quantities			
Name	Unit	Value	Error
P_2	[d]	4941	191
RMS	[min]	1.382	0.197
$Pdot$	[d/yr]	-1.095×10^{-6}	0.072×10^{-6}
$Ampl$	[min]	11.007	0.484

Notes: For the meaning of the regression coefficients $\{c_i\}$ see Fig. B.1. Errors on $\{c_i\}$ are *full* standard deviations (i.e., including fitting error from P_2). The RMS of the fit is unbiased, but omitting the correction to the 6-th parameter P_2 . In the MCMC process RMS and $Pdot$ are fitted parameters and the related $\{c_i\}$ values are computed from these.

Science Archive⁶. This yields: $E(B - V) = 0.082 \pm 0.002$. Extinction in any given waveband has been computed by $A_\lambda = R_\lambda E(B - V)$, where the extinction coefficients R_λ given by Yuan, Liu & Xiang (2013), Sanders & Das (2018), Liu & Janes (1990) and Davenport et al. (2014) were used. For the XMM-Newton UVW1 band, we employed the York Extinction Solver⁷ (see McCall 2004). All these input data to construct the observed SED for KIC 9832227 (see Fig. 9) are listed in Table C.1.

We note that the reddening value for KIC 9832227 is far from accurate – in spite of the small formal error bar of the value we used. Molnar et al. (2017) compare the spectroscopic and color-calibrated T_{eff} values to derive a considerably lower value of $E(B - V) = 0.030 \pm 0.002$. The *MWDust* tool by Bovy et al. (2016) yields $E(B - V) = 0.021$. Exceeding all these values, by using the extinction coefficients of Wang & Chen (2019), the Gaia catalog yields $E(B - V) = 0.291$ or 0.318 for the 68% lower limits, depending if we use their $E(BP - RP)$ or A_G values. Although these large values are clearly incompatible with the SED based on the accurate distance of the system, it is unclear if some considerably lower value than the one we adopted is strongly justifiable by the present data.

Transformation to the Vega system has been performed in the following way. When the observed magnitudes were given in the AB system (i.e., for GALEX, XMM, M17), we computed $m(\text{Vega}) = m(\text{AB}) + 2.5 \log(ZP/3631)$, where the zero point ZP for the given waveband was taken from the Spanish Visual Observatory site. The Gaia and the WISE magnitudes are defined on the Vega system⁸, so their observed and transformed values are the same. The APASS magnitudes are in the Johnson system, that can be transformed to the AB system based on Frei & Gunn (1994)⁹. Then, these magnitudes were transformed to the Vega system as already mentioned above. The 2MASS magnitudes are nearly on the Vega system, but, according to Apellaniz & Gonzalez (2018), there might be some systematic differences, yielding the following shifts to the published values: $J(\text{Vega}) = J(\text{publ}) - 0.025 \pm 0.005$, $H(\text{Vega}) =$

Table C.1. Observed magnitudes of KIC 9832227.

Source	Band	Band (μm)	Range (μm)	Obs (mag)	Vega (mag)	Error (mag)	R_λ
GALEX	NUV	0.232	0.037	17.522	15.855	0.012	7.24
XMM	UVW1	0.298	0.040	15.208	13.876	0.002	5.60
M17	g	0.472	0.058	12.721	12.817	0.001	3.31
M17	r	0.619	0.056	12.279	12.129	0.001	2.32
M17	i	0.750	0.052	12.171	11.809	0.001	1.72
M17	z	0.896	0.056	12.157	11.635	0.001	1.28
GAIA	G	0.674	0.210	12.293	12.293	0.005	2.39
GAIA	BP	0.532	0.117	12.626	12.626	0.015	3.17
GAIA	RP	0.799	0.142	11.820	11.820	0.015	1.81
APASS	B	0.431	0.042	13.081	13.023	0.121	4.10
APASS	V	0.545	0.044	12.351	12.305	0.087	3.10
2MASS	J	1.235	0.081	11.298	11.273	0.021	0.72
2MASS	H	1.662	0.125	11.033	11.037	0.017	0.46
2MASS	K	2.159	0.131	10.998	10.983	0.016	0.31
WISE	W1	3.353	0.331	10.921	10.921	0.023	0.19
WISE	W2	4.603	0.521	10.946	10.946	0.021	0.15
WISE	W3	11.561	2.753	10.865	10.865	0.072	0.30
WISE	W4	22.088	2.051	9.492	9.492	9.999	0.08

Notes: Magnitudes are *not* corrected for reddening. Further details on items entering in this table can be found in Appendix C.

$H(\text{publ}) + 0.004 \pm 0.005$, $K(\text{Vega}) = K(\text{publ}) - 0.015 \pm 0.005$. We applied these corrections to the observed 2MASS magnitudes.

The theoretical SEDs have been downloaded from the Spanish Visual Observatory site¹⁰, using the grid closest to the observed parameters. For the binary components we used the $T_{\text{eff}} = 6000$ K and 5750 K models, both with solar composition, $\log g = 4.0$, mixing length and microturbulence velocity of 1.25 and 2 km/s, respectively. These models are without convective overshooting (see Castelli, Gratton & Kurucz 1997). The current Gaia distance of 585 ± 10 pc and the radii of Molnar et al. (2017) ($1.58 R_\odot$ and $0.83 R_\odot$ for the primary and secondary component, respectively) were used to compute the predicted fluxes. In one scenario, the third component was assumed to be a $T_{\text{eff}} = 3500$ K, $R = 0.4 R_\odot$ main sequence star, whereas in another scenario it was assumed to be a white dwarf with $T_{\text{eff}} = 30000$ K, $\log g = 8.0$ and $R = 0.016 R_\odot$. In this latter scenario, we used the stellar atmosphere models of Koester (2010) downloaded from the site cited above. The parameters for the white dwarf model are broadly consistent with the model values of Romero et al. (2019) at the temperature chosen, and assuming a mass of $M \sim 0.49 M_\odot$. This stellar mass is above by $0.11 M_\odot$ of our minimum value derived from the light time effect (see Sect. 4).

⁶ <https://irsa.ipac.caltech.edu/applications/DUST/>

⁷ <http://www.cadc-ccda.hia-ihp.nrc-cnrc.gc.ca/community/YorkExtinctionSolver/output.cgi>

⁸ For Gaia, see the VizieR site, for WISE, see: <http://wise2.ipac.caltech.edu/docs/release/allwise/faq.html>

⁹ See also <http://astroweb.case.edu/ssm/ASTR620/mags.html> ¹⁰ <http://svo2.cab.inta-csic.es/theory/newov2/>